RSC Advances

PAPER

View Article Online
View Journal | View Issue

Cite this: *RSC Adv.*, 2026, **16**, 8709

Pechini synthesis and characterization of Co_2MnO_4 nanostructures and their application as a nano-photocatalyst for degradation of malachite green in contaminated water under sunlight

Masoumeh Yaqoubi,[a] Mojgan Ghanbari,[a] Elmuez A. Dawi,[b] Safaa H. Ganduh,[c] Layth S. Jasim[d] and Masoud Salavati-Niasari*[ae]

A spinel-type Co_2MnO_4 nanostructure was synthesized under various chelating and polymerizing conditions and systematically investigated for its ability to degrade malachite green (MG) in visible light. The structural, morphological, and optical properties of the samples were analyzed using XRD, FTIR, FESEM, EDX, TEM, BET, and DRS techniques. In this study, the catalyst synthesized from citric acid and propylene glycol (CMO-1) was most effective, with a generally uniform morphology and narrow particle size distribution (100–120 nm), a high surface area and a narrow 1.52 eV bandgap, among all samples examined. Under visible light, CMO-1 minimally degraded MG by 98.6% in 120 minutes with pseudo-first-order kinetics (k = 0.02542 min^{-1}). In scavenger experiments, it was determined that photogenerated holes (h^+) contributed the most to degradation. Furthermore, the stability of the catalyst was assessed, in which it maintained 85% activity after 5 consecutive cycles of degradation without deteriorating structurally. A comparison of Co_2MnO_4 with other manganese-based and composite photocatalysts revealed similar or better performance when activated by visible light, demonstrating its potential as an effective and reusable photocatalyst for wastewater treatment.

Received 20th November 2025
Accepted 6th February 2026

DOI: 10.1039/d5ra08965d

rsc.li/rsc-advances

1. Introduction

The rapid proliferation of synthetic dyes in fields such as textiles, leather, paper, and plastics represents a significantly deep concern for the environment due to their organic release, which is typically highly stable and non-biodegradable organic contaminants into aquatic systems.[1,2] As a result of their toxic, mutagenic, and relatively persistent nature, these contaminants are often considered hazardous to ecosystems and human health.[3] Among the various methods established for wastewater treatment, semiconductor-based photocatalysis offers a green, relatively efficient, and practical approach to degrading organic contaminants under light irradiation.[4]

This process relies heavily on photocatalytic materials, and as such, the photocatalytic and charge transport properties of a photocatalytic material will determine the overall efficiency of the system and, ultimately, whether it is viable or useful for its intended application.[5] Transition metal oxides, in particular, spinel-type transition metal oxides, have recently garnered research attention due to their structural stability, synthesis easiness, and the presence of redox-active cations.[6,7]

Cobalt manganese oxide, Co_2MnO_4 (CMO), is a member of the spinel group of materials that has intriguing structural and electronic properties that have made it extremely interesting to the materials community. Interest in Co_2MnO_4 has burgeoned in the last decade due to its focus on catalysis from a materials science perspective, specifically in the area of oxygen reduction and evolution reactions.[8] Co_2MnO_4 demonstrates excellent electrocatalytic activity, leading the material to be exploitable in several energy conversion technologies such as metal–air batteries and proton exchange membrane electrolyzers.[9] In addition, Co_2MnO_4 can be modified in a variety of ways, such as by doping it with other elements to enhance its stability and catalytic properties.[10] Besides its catalysis applications, Co_2MnO_4 has also been investigated for its magnetoelectric properties, which could be applied to advanced electronic devices.[11] Spinal-type oxide of cobalt and manganese, on the other hand, has a narrow energy level gap at the time of reacting

[a]*Institute of Nano Science and Nano Technology, University of Kashan, P. O. Box 87317-51167, Kashan, Iran. E-mail: Salavati@kashanu.ac.ir; Fax: +98 31 55913201; Tel: +98 31 55912383*

[b]*College of Humanities and Sciences, Department of Mathematics and Sciences, Ajman University, P. O. Box 346, Ajman, United Arab Emirates*

[c]*Department of Chemistry Pharmaceutical, College of Pharmacy, University of Al-Qadisiyah, Diwaniyah, Iraq*

[d]*Department of Chemistry, College of Education, University of Al-Qadisiyah, Diwaniyah, Iraq*

[e]*Department of Inorganic Chemistry, Faculty of Chemistry, University of Kashan, P. O. Box 87317-51167, Kashan, Iran*

with photocatalysts and oxidants, as well as having mixed oxidation–reduction centers, which can be used for producing materials that absorb visible light and separate positive and negative charge carriers.[12] The performance of nanomaterials largely relies on their thermal history since the heating and cooling processes can greatly affect phase stability, structure, and surface characteristics.[13] Previous work using cobalt-manganese oxide-related materials (*e.g.*, $CoMn_2O_4$ and $NiMn_2O_4$) has demonstrated the efficiency of olympic green degradation as being between 60 and 91% under either visible or solar radiation, with most energy gaps exceeding 1.7 eV.[14–16] On the other hand, Co_2MnO_4 has a smaller energy gap (approximately 1.5–1.7 eV) and exhibits greater electrical conductivity, due in part to the synergistic effect of Co/Mn mixed oxidation–reduction systems,[17] thus providing Co_2MnO_4 an even better photocatalytic potential than that of Co/Mn-related materials. Based on the above description of the physical and chemical properties of Co_2MnO_4, as well as the extensive application of Co_2MnO_4 in electrocatalysis, the current research is one of the first reports to systematically evaluate the visible light photocatalytic activity of Co_2MnO_4 as an organic dye decomposer. Co_2MnO_4 represents a very flexible material that provides the potential to help advance sustainable energy solutions and materials science engineering. In spite of the fact that Co_2MnO_4 has been studied for its chemical properties and used in several applications, the photocatalytic degradation of organic pollutants has not been fully documented in literature. This presents an opportunity to investigate and characterize the photocatalytic behavior of Co_2MnO_4 for photocatalytic degradation as a new photocatalyst for environmental remediation.

Co_2MnO_4 nanoparticles were made for this study using a modified Pechini method with the intention of changing particle morphology to create a direct correlation between synthesis conditions and their visible light-driven photocatalytic activity toward degrading malachite green dye through systematic experimentation. This is the first time, to our knowledge, that there has been a comprehensive evaluation of the influence that Pechini synthesis variables have on producing efficient photocatalysts for the visible light degradation of malachite green dye and creating advanced spinel type photocatalysts that can be used effectively in water treatment.

2. Materials and methods

2.1. Materials

Cobalt(II) acetate tetrahydrate, 98% ($Co(CH_3COO)_2 \cdot 6H_2O$), manganese nitrate tetrahydrate 98.0% ($Mn(NO_3)_2 \cdot 4H_2O$), citric acid (CA) 99.5%, succinic acid (SA) 99%, 1,4-benzoquinone 98% (BQ), malonic acid (MA) 99%, propylene glycol (PG) 99.9%, ethylenediaminetetraacetic acid 99% (EDTA), ethylene glycol (EG) 99.9%, glycerol (Gly) 95%, Eriochrome Black-T (EBT), rhodamine B (RB), malachite green (MG), methyl orange (MO), benzoic acid 99.99% (BA), methyl violet (MV), and eosin Y (EY) were obtained from Sigma-Aldrich and used as received without further purification.

Table 1 Preparation condition of Co_2MnO_4 nanostructures

Grain size (nm)	Polymerizing agent	Chelating agents	Sample code	Sample no.
28.55	PG	CA	CMO-1	1
22.66	PG	MA	CMO-2	2
29.55	PG	SA	CMO-3	3
28.11	Gly	CA	CMO-4	4
26.88	EG	CA	CMO-5	5

2.2. Preparation of Co_2MnO_4

1.0 mmol of $Co(CH_3COO)_2$ was dissolved in 10 mL of deionized water in separate beakers. Separately, 210 mg of CA (118 mg of SA or 104 mg of MA) was diluted in 10 mL of water. The CA (SA or MA) solution was then added to the Co^{2+} solution and stirred for 20 minutes. After that, 1.0 mmol of $Mn(NO_3)_2$ was dissolved in 10 mL of deionized water and introduced into the mixture. The resulting solution was stirred for 30 minutes until a clear solution was obtained. Next, 1.0 mmol of PG (EG or Gly) was added, stirring for another 20 minutes. The temperature was then increased to 90–110 °C to evaporate the solvent and form a gel. The resulting gel was dried in an oven at 50 °C for 24 hours. Finally, the dried gel was calcined in a furnace at 700 °C for 3 hours to produce Co_2MnO_4 nanoparticles. The various conditions for synthesizing Co_2MnO_4 nanoparticles are indicated in Table 1.

2.3. Photocatalytic operation

A 100 mL dye solution, including MV, MO, EY, RB, MG, and EBT with a concentration of 10 mg L^{-1} was combined with 30 mg of Co_2MnO_4 in a quartz cell. The mixture was stirred in the dark for 30 minutes to allow the adsorption–desorption equilibrium to be established. During the photocatalytic experiment, the solution was exposed to visible light from a 200 W OSRAM lamp to generate photon energy. At regular intervals, 3 mL samples were withdrawn from the mixture, centrifuged, and analyzed using a UV-Vis spectrophotometer. The photocatalytic degradation efficiency was calculated based on the concentration of the dye at time t (C) relative to the initial equilibrium concentration (C_0) measured at time t_0.[18]

$$E(\%) = \left(1 - \frac{C}{C_0}\right) \times 100 \quad (1)$$

3. Results and discussion

3.1. Characterization

X-ray diffraction (XRD) analysis was performed to assess the crystal structure of the Co_2MnO_4 nanostructures synthesized under distinct preparation conditions (Fig. 1). The diffraction peaks in all samples were clear according to the method used, which indicated a spinel structure of Co_2MnO_4 with the most intense reflections located at approximately $2\theta = 18.7°$, 30.6°,

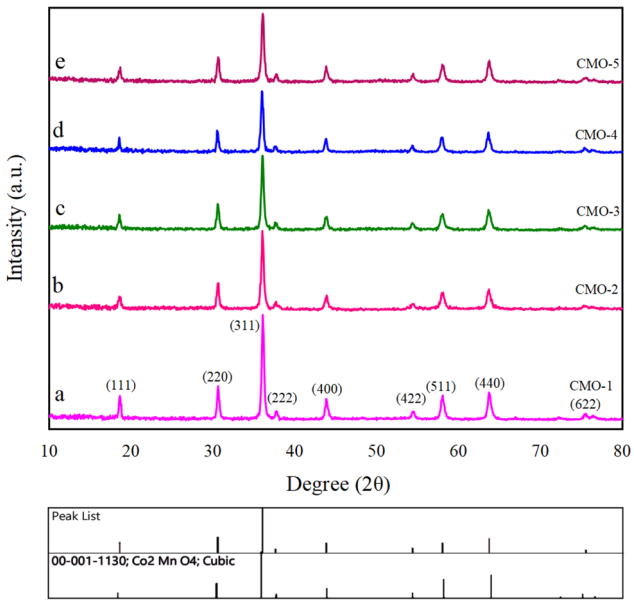

Fig. 1 XRD patterns of as-prepared samples in different conditions according to Table 1, (a) CMO-1, (b) CMO-2, (c) CMO-3, (d) CMO-4, and (e) CMO-5.

36.1°, 37.8°, 43.8°, 54.5°, 58.1°, 63.7°, and 75.6°, corresponding to the (111), (220), (311), (222), (400), (422), (511), (440), and (622) planes respectively. It was determined that the results were consistent with the card number (JCPDS no. 00-001-1130). Crystallite sizes, which were calculated *via* the Scherrer equation, were, for example, CMO-1 $D = 28.55$ nm; CMO-2 $D = 22.66$ nm; CMO-3 $D = 29.55$ nm; CMO-4 $D = 28.11$ nm; and CMO-5 $D = 26.88$ nm. The smallest crystallite size of 22.66 nm was found on CMO-2 and can likely attributed to the stronger chelating properties of malic acid (MA). CMO-1 had a very respectable size and was the most uniform and dispersed, which would provide positive or additional benefits as the following morphology and performance experimental data illustrated.

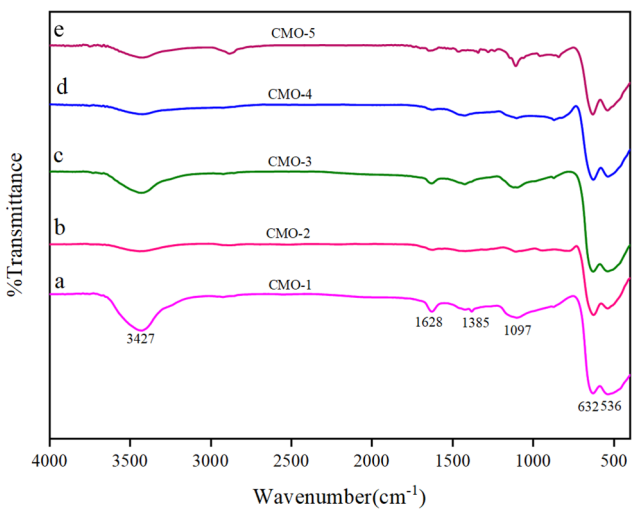

Fig. 2 FTIR spectra of as-prepared samples in different conditions according to Table 1, (a) CMO-1, (b) CMO-2, (c) CMO-3, (d) CMO-4, and (e) CMO-5.

FTIR spectroscopy provided additional evidence for the formation of the spinel structure of all of the spectra (Fig. 2), showing the metal–oxygen stretching vibrations characteristic of Co–O or Mn–O bonds between 530 and 630 cm^{-1}.[19,20] The broad bands at 3427 cm^{-1} and the sharp band at 1628 cm^{-1} were also observable, corresponding to O–H stretching or bending vibrations from the small amounts of water molecules that are adsorbed on the surface of the metals.[21] A weak band around 1385 cm^{-1} can also be identified that can be attributed to residual organic species. Although there were no identifiable significant peaks to any organic compounds, the lack of substantial peaks indicated that the precursors had been adequately decomposed.

FESEM imaging was used to confirm the structure of the synthesized Co_2MnO_4 nanostructures, revealing substantial variation between them depending on the chelating and polymerizing agents used during synthesis. Sample CMO-1 (Fig. 3a), which is synthesized using citric acid and propylene glycol, exhibited a very uniform morphology of near-spherical, well-dispersed nanoparticles with minimal aggregation, suggesting that coordination and polymerization were effectively controlled during the synthesis. Citric acid likely had a strong chelating effect, and propylene glycol had a moderate viscosity, which together developed homogeneous nucleation and growth. Sample CMO-2 (Fig. 3b) was synthesized with malonic acid and propylene glycol and showed smaller particle sizes with a slightly rougher surface and less uniformity with some clustering of particles, indicating malonic acid induces less steric stabilization than citric acid. Sample CMO-3 (Fig. 3c) using succinic acid showed the poorest morphology, with concentrated areas of agglomeration with poorly defined particle borders, indicating weak complexation with succinic acid and uncontrolled gelation. Sample CMO-4 (Fig. 3d), which was made with glycerol instead of propylene glycol, showed larger and more aggregated particles, which is likely due to the high viscosity of glycerol and multiple hydroxyl groups that likely interfered with uniform gel formation. Lastly, the morphology of CMO-5 (Fig. 3e), derived *via* citric acid and ethylene glycol, showed moderately uniform morphology with semi-spherical particle shapes and some moderate aggregation. Although CMO-5's morphology was better than CMO-3 and CMO-4, CMO-5's morphology was still a step down from CMO-1, establishing the dual significance of chelating and polymerizing agents as controls of nanoparticle morphology. Therefore, CMO-1, because of its most uniform and dispersed morphology due to the increased surface access, was the best potential microstructure for photocatalytic use.

FESEM images and Digimizer software were used to obtain particle size distributions of Co_2MnO_4 nanostructures, which provided insight into the effects of synthesis conditions on particle uniformity and dispersion. The histograms (Fig. 4a–e) indicated that there were considerable differences among the five samples (CMO-1 to CMO-5). The particle size for CMO-1 was narrow and fairly symmetrical, with most particle size between 80 to 140 nm; the mode was generated in the 100–120 nm range.

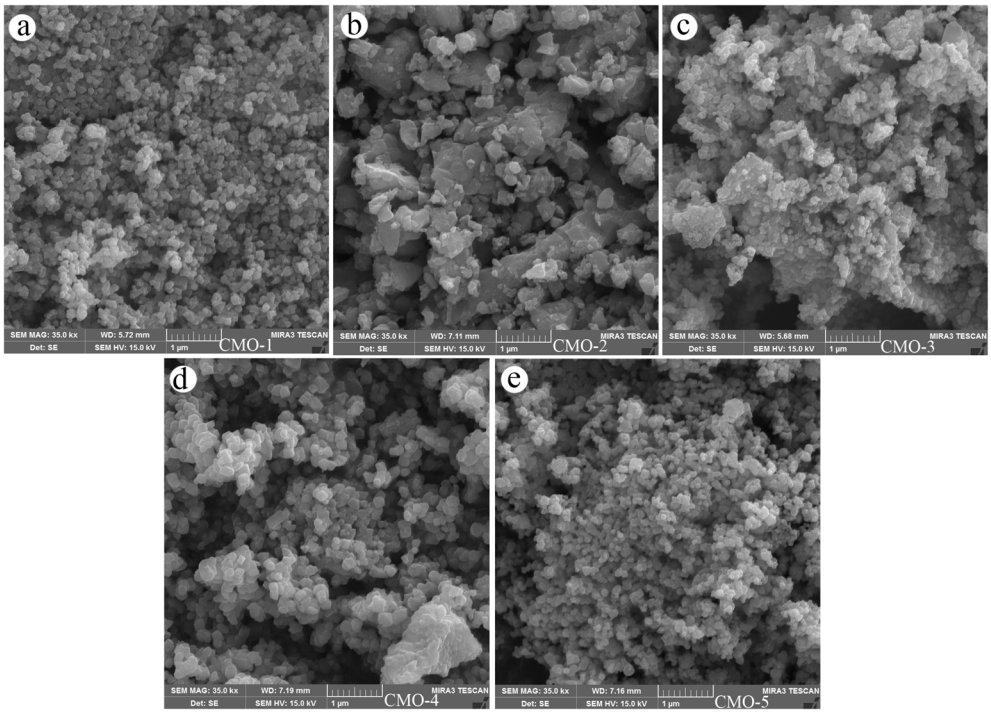

Fig. 3 FESEM images of Co_2MnO_4 nanostructures synthesized under different conditions: (a) CMO-1, (b) CMO-2, (c) CMO-3, (d) CMO-4, and (e) CMO-5. All images were recorded at the same magnification; scale bar = 1 μm.

The narrow particle distribution is indicative of controlled nucleation and growth processes that yield uniform morphology and limited coalescence of nanostructures. In the photocatalytic application, the narrow distribution of particle size corresponds to homogeneous morphology, which ensures uniform reactive surface areas and better charge carrier mobility. On the other hand, CMO-2 had a distribution that covered a larger size range (80–200 nm), whereas the modal distribution was in the size range of 120–160 nm. CMO-2 had a relatively uniform particle size distribution, but the

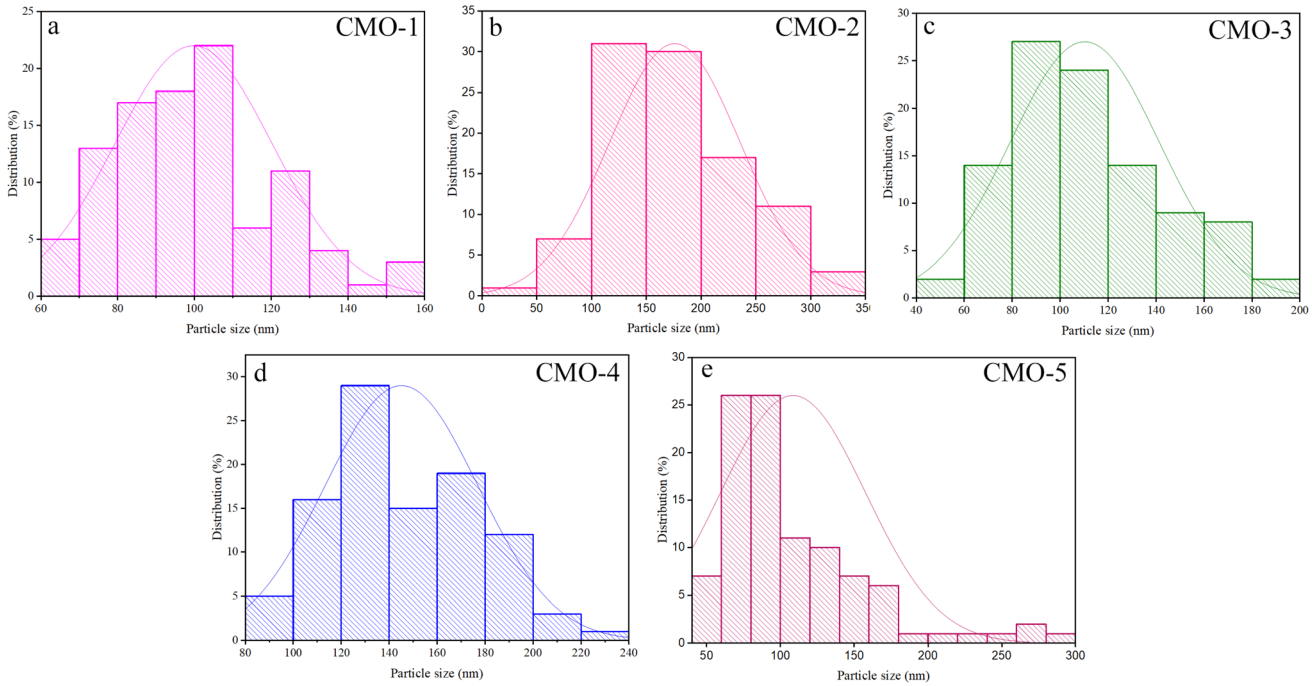

Fig. 4 Size distribution diagram of as-prepared samples in different conditions according to Table 1 obtained from corresponding FESEM images. (a) CMO-1, (b) CMO-2, (c) CMO-3, (d) CMO-4, and (e) CMO-5.

appearance of slightly larger particles may indicate partial aggregation or secondary growth, likely due to malonic acid's weaker chelating effect than citric acid. This increased range of particle sizes may have a small effect on the consistency of surface activity. CMO-3 had a similar average size range (approximately 60–180 nm), but it had more evident size variation and tailing toward the larger particles. The occurrence of particles larger than 160 nm indicates that there was quite a bit of agglomeration present and less uniformity in CMO-3 compared to CMO-2. The FESEM images revealed fused structures, which further supports that there was significant aggregation, likely as a result of minimal control of the synthesis by employing succinic acid as the chelating agent. The distribution of CMO-4 was even greater, with a range of approximately (80–240 nm) and decidedly asymmetrical. The significant number of larger particles indicates that there was an even higher degree of polydispersity than CMO-2 or CMO-3. The polydispersity can be attributed to the polymerizing agent, glycerol. The high viscosity of glycerol may impede effective diffusion and gelation and consequently become problematic for particle growth where unevenness and aggregation may become prevalent. Among the samples, CMO-5 had the widest distribution spanning particle size from under 50 nm to over 300 nm. While most particles were below 150 nm in size, the very strong tail to larger sizes indicates that particles were formed heterogeneously either because of incomplete complexation in solution or localized sintering in the bulk of the material during calcination. Such a degree of polydispersity leads to reductions in photocatalytic performance because of the chances of inconsistent surface area and reactivity. Overall, the narrow and well-centered size distribution of CMO-1 further validates its particle uniformity and control in the synthesis this sample also supported improved photocatalytic performance. Comparatively, the broader and more irregular distributions of CMO-4 and CMO-5 indicated less controlled synthesis conditions that threaten the photocatalyst efficiency and stability.

Energy-dispersive X-ray spectroscopy (EDS) with elemental mapping was performed to evaluate the elemental compositions and spatial distribution of cobalt (Co), manganese (Mn), and oxygen (O) in synthesized Co_2MnO_4 nanostructures (Fig. 5). The EDS spectra for all samples showed detectable elements representative of the stoichiometry and no related impurities, thereby corroborating the successful synthesis and high chemical purity of the spinel. However, variations in the homogeneity of the elemental distribution were observed among the samples. The EDS elemental mapping for CMO-1, synthesized using citric acid and propylene glycol, revealed a highly uniform and homogeneous distribution of Co, Mn, and O on the entire particle surface. This even distribution is likely due to effective chelation with the citric acid and the formation of homo-polymerization with the propylene glycol during the synthesis of CMO-1. As a result of the elemental mapping, the EDS quantitative analysis of all elements revealed that the Co : Mn ratio was very close to 2 : 1, thereby confirming the successful stoichiometric synthesis of Co_2MnO_4 and the structural integrity of the CMO-1 sample. The mapping of CMO-2, synthesized with malonic acid as a chelating agent, also showed primarily good distribution of the elements, although there were some increased localized intensities in the elemental Mn signal intensity, which may indicate mild inhomogeneity, with the potential of small Mn-rich domains. This may be due to malonic acid's less strong complexing capacity, which can influence the overall uniformity of the various metal ions' coordination while the gelation progresses. The CMO-3 sample produced from succinic acid showed the least favorable elemental, or even spatial, uniformity. The Co and Mn data also appeared more aggregated, and some of the regions were enriched in one element over the other. This disparity in distribution can be understood as inefficient molecular-level coordination and mixing, which resulted in spatial compositional heterogeneities that may be inhibiting crystallinity and photocatalytic activity. For the CMO-4 sample (citric acid and glycerol), the elemental mapping indicated a moderately uniform distribution, although it was more aggregated compared to CMO-1. The viscosity of glycerol could have inhibited more effective mixing and diffusion of the metal ions, therefore producing varying concentrations of the element in discrete areas during synthesis. CMO-5 (citric acid and ethylene glycol) displayed reasonably uniform Co, Mn, and O distribution; an improvement over the CMO-3 and CMO-4 samples. Although it was not homogenous like in CMO-1, some tiny differences in signal intensity of the coatings indicate some aggregation, most likely during synthesis, attributed to ethylene glycol having a lower molecular weight, hindering the effective coordination size and steric hindrance.

Transmission Electron Microscopy (TEM) images of CMO-1 corroborated the FESEM findings, revealing nanoparticles with diameters ranging from 80 to 100 nm, confirming the results obtained from FESEM images (Fig. 6).

An analysis of the BET surface area was conducted in order to investigate the textural properties. The nitrogen adsorption–desorption isotherm of CMO-1 displayed a type IV isotherm with an H3 hysteresis loop (Fig. 7a) indicative of mesoporous materials. The BJH pore size distribution (Fig. 7b) showed the existence of mesopores in the size range of 2–20 nm. These porous structures are useful for increasing surface active sites and promoting diffusion of reactants during photocatalytic reactions. The BET data yields the total pore volumes (p/p_0 = 0.940) of 0.0075271 $cm^3\ g^{-1}$, a specific surface area of 3.304 $m^2\ g^{-1}$, and the mean pore diameters of 9.1127 nm.

To study the optical absorption behavior and band gap energy of Co_2MnO_4 (CMO-1 to CMO-5), diffuse reflectance spectroscopy (DRS) was performed on all CMO samples (Fig. 7(c–l)). All samples showed the same strong response to visible light, which corresponds with the narrow band gap nature of spinel Co_2MnO_4. Tauc plots of the samples indicate that the band gap of the samples was approximately 1.51–1.52 eV, which have very little variation, indicating that the photocatalytic performance and the property of optical absorption do not control the difference in the samples' performance. This suggests other factors, such as morphology, variation in particle size distribution, surface area, and structural homogeneity, may play a more significant role in determining the difference in the samples' photocatalytic performance. This

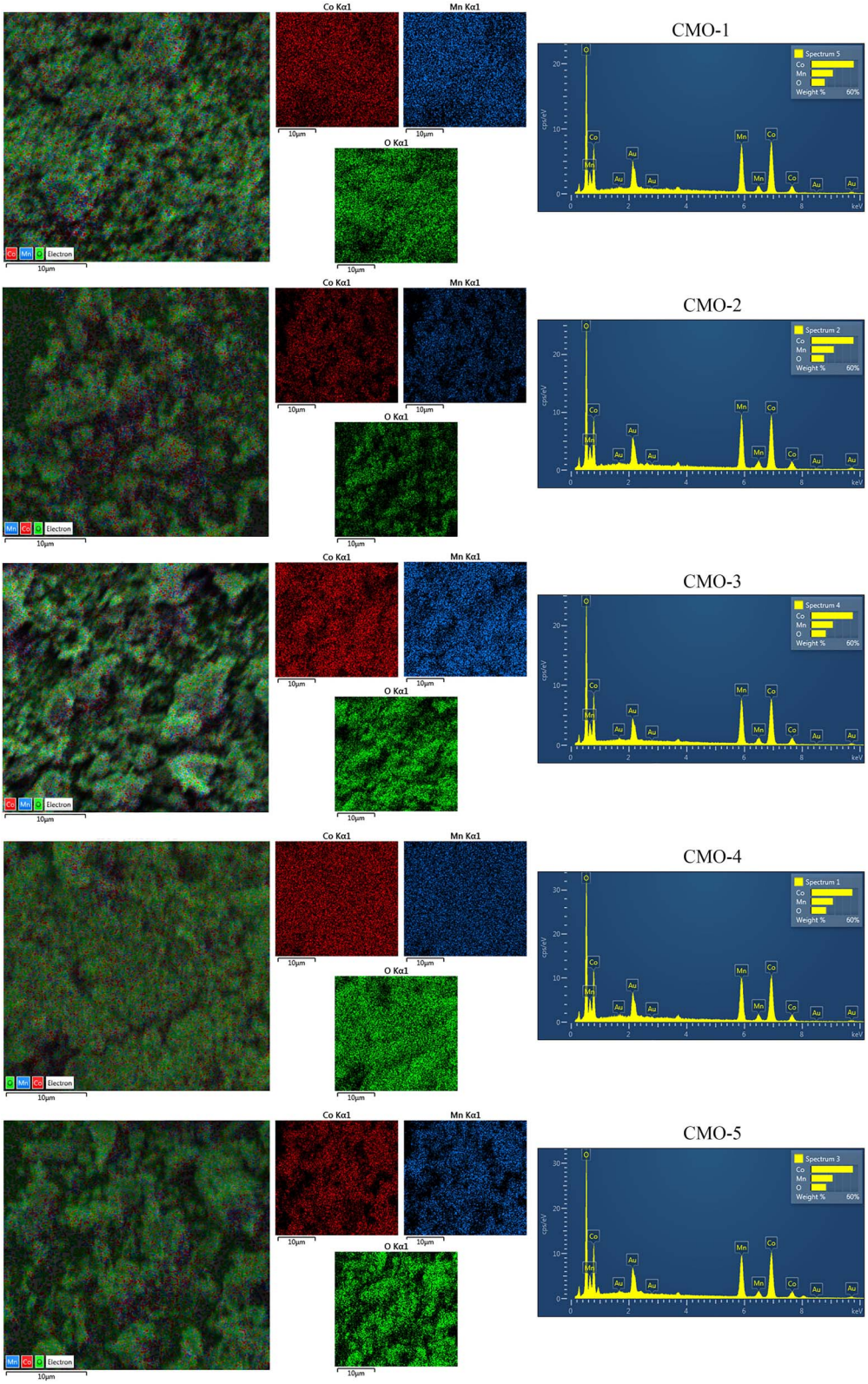

Fig. 5 Elemental mapping and EDX analysis of as-prepared samples in different conditions according to Table 1.

finding suggests that the high performance of the optimized sample is likely due to good charge separation efficiency and greater access to surface-active sites, not narrowed band gap.

3.2. Photocatalytic efficiency

The photocatalytic activity of the synthesized Co_2MnO_4 nanostructures was examined through the degradation of organic

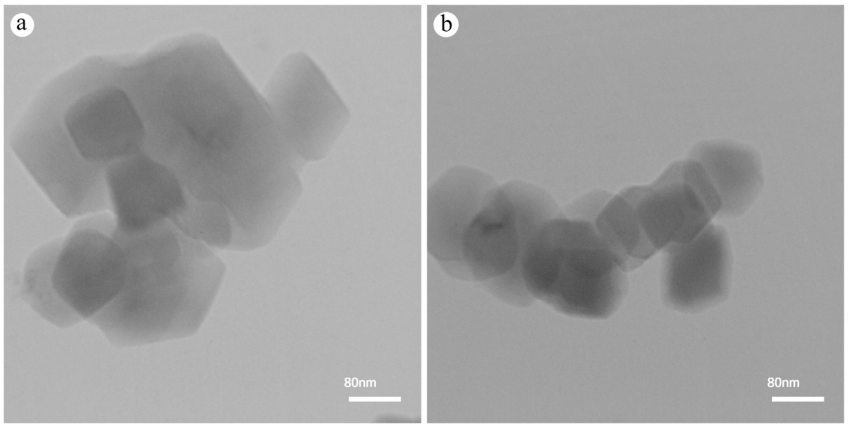

Fig. 6 (a and b) TEM images of Co_2MnO_4 prepared in the presence of CA and PG (CMO-1) recorded at same magnifications and scale bar of 80 nm.

dyes, especially malachite green (MG) under visible light irradiation, and several factors were assessed to inform our understanding of the photocatalytic behavior (the incidence of these conditions including the synthesis conditions, type of dye, initial dye concentration, catalyst dosage, composition of solution, as well the contribution of active species were examined). In Fig. 8a, photocatalytic efficiencies of five Co_2MnO_4 samples (CMO-1⋯CMO-5) were compared under identical conditions (30 mg of catalyst and 10 ppm MG solution). In all the samples, CMO-1 exhibited the highest degradation efficiency (98.6% degradation) after 90 minutes of irradiation. This is attributed to the differences in morphology, crystallinity, and distribution of species. The differences in the remaining samples were ranked as follows: CMO-2 (75.7%) > CMO-3 (67.6%) > CMO-5 (63.5%) > CMO-4 (57.8%). The differences in performance are based on their morphological differences and degrees of homogeneity as discussed earlier. Particle size is a highly important factor in photocatalytic function. Smaller and more

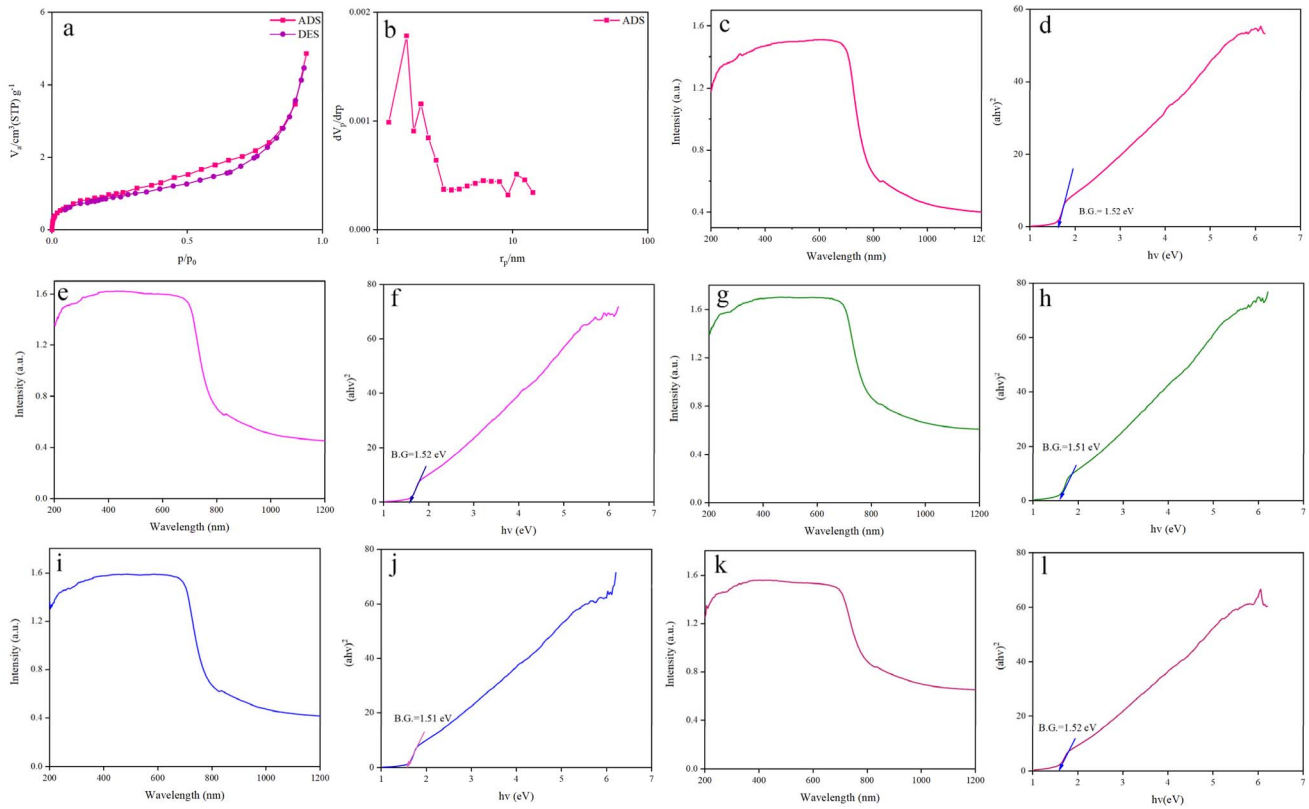

Fig. 7 (a) N_2 adsorption–desorption isotherm, (b) BJH plot, DRS spectrum and Tauc plot of Co_2MnO_4 prepared in different conditions (c and d) CMO-1, (e and f) CMO-2, (g and h) CMO-3, (i and j) CMO-4, and (k and l) CMO-5.

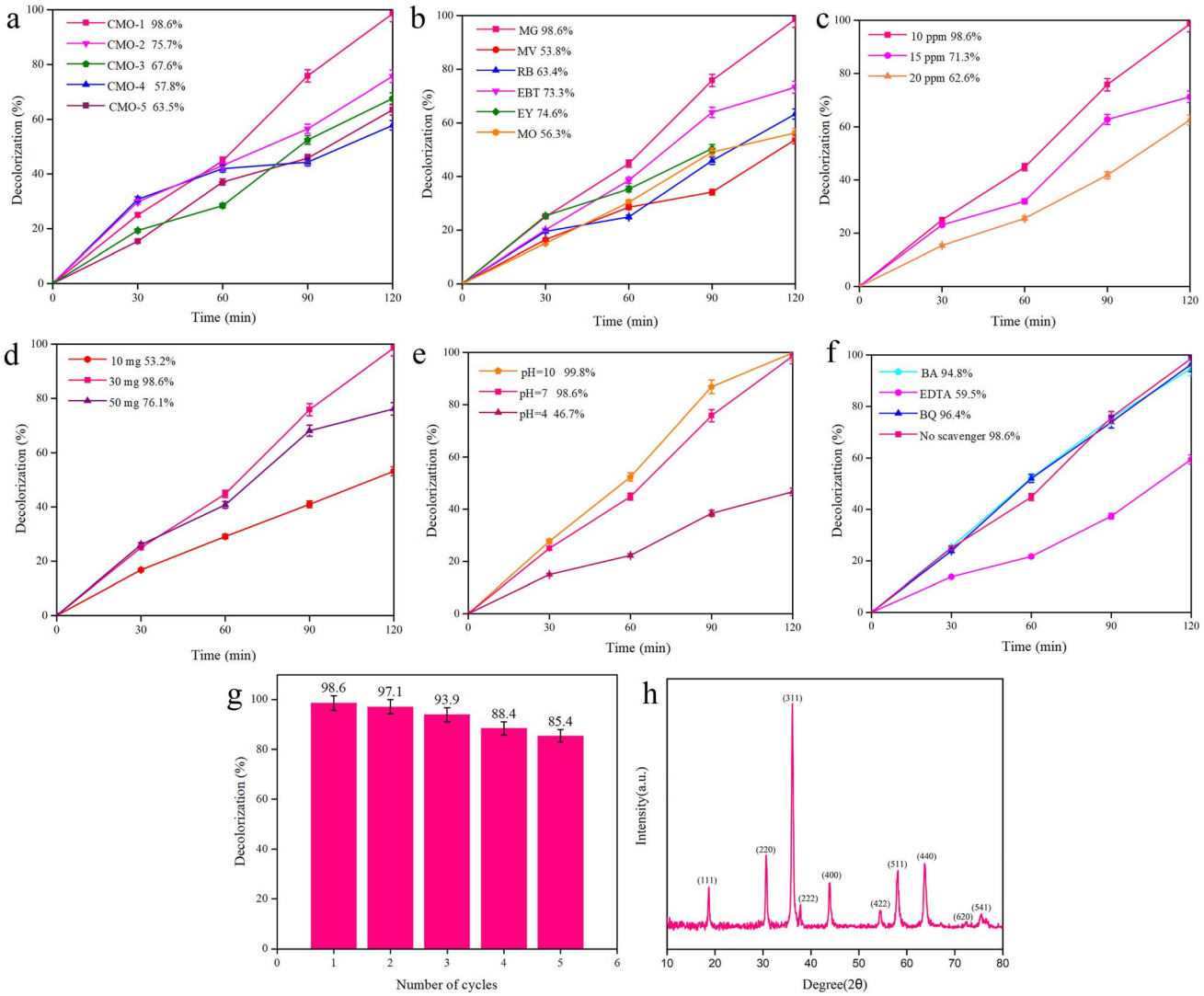

Fig. 8 Photocatalytic performance of (a) different samples of Co_2MnO_4 prepared in different conditions, (b) effect of different organic dyes, (c) effect of different MG concentrations in the presence of 30 mg Co_2MnO_4 prepared in the presence of CA and PG, (d) effect of different dosages of Co_2MnO_4 prepared in the presence of CA and PG over 10 ppm MG, (e) effect of various pH solution, and (f) effect of different scavengers, (g) recyclability test, and (h) XRD pattern after five cycle degradation over Co_2MnO_4 prepared in the presence of CA and PG under visible light.

uniformly sized particles, like those found in CMO-1, result in a much larger effective surface area, shorter diffusion distances for charge carriers, and a lower probability of recombination between electrons and holes than do larger particle sizes or groups of particles that have formed by agglomeration; larger or agglomerated particle sizes will have fewer active sites available and greater amounts of bulk recombination occurring, hence causing degraded rates of degradation. Thus, the superior performance of CMO-1 as a photocatalyst can be directly attributed to its optimal particle diameter and to its uniformity of morphology. Fig. 8b demonstrates the influence of different dyes on the photocatalytic activity of CMO-1. CMO-1 exhibited its effective degradation efficiency in the following order: MG (98.6%) > EY (74.6%) > EBT (73.3%) > RB (63.4%) > MO (56.3%) > MV (53.8%). The trend can be attributed to varying molecular structure, adsorption affinity, and light absorption properties of the dyes. MG has a strong interaction with the surface of the catalyst and more light absorption in the visible region, which leads to better photocatalytic degradation.

The effect of the initial concentration of MG (10–20 ppm) on degradation performance is shown in Fig. 8c (using a consistent amount of catalyst amount of 30 mg CMO-1). The results indicated that degradation efficiencies decreased with increasing dye concentration. At 10 ppm, degradation was almost complete at 98.6%, while the degradation efficiency dropped to 62.6% at 20 ppm. The reason for activity reduction at elevated concentrations can be explained by two key factors (i) increased optical density of the solution that reduces light penetration and therefore, limited-photon absorption by the catalyst and (ii) dye molecules adsorbing excess numbers on catalytic sites, once again saturation occurs with active sites exposed on the catalyst surface.[22]

The effect of catalyst dosage on MG degradation is shown in Fig. 8d. The degradation experiment with a 10 ppm MG solution

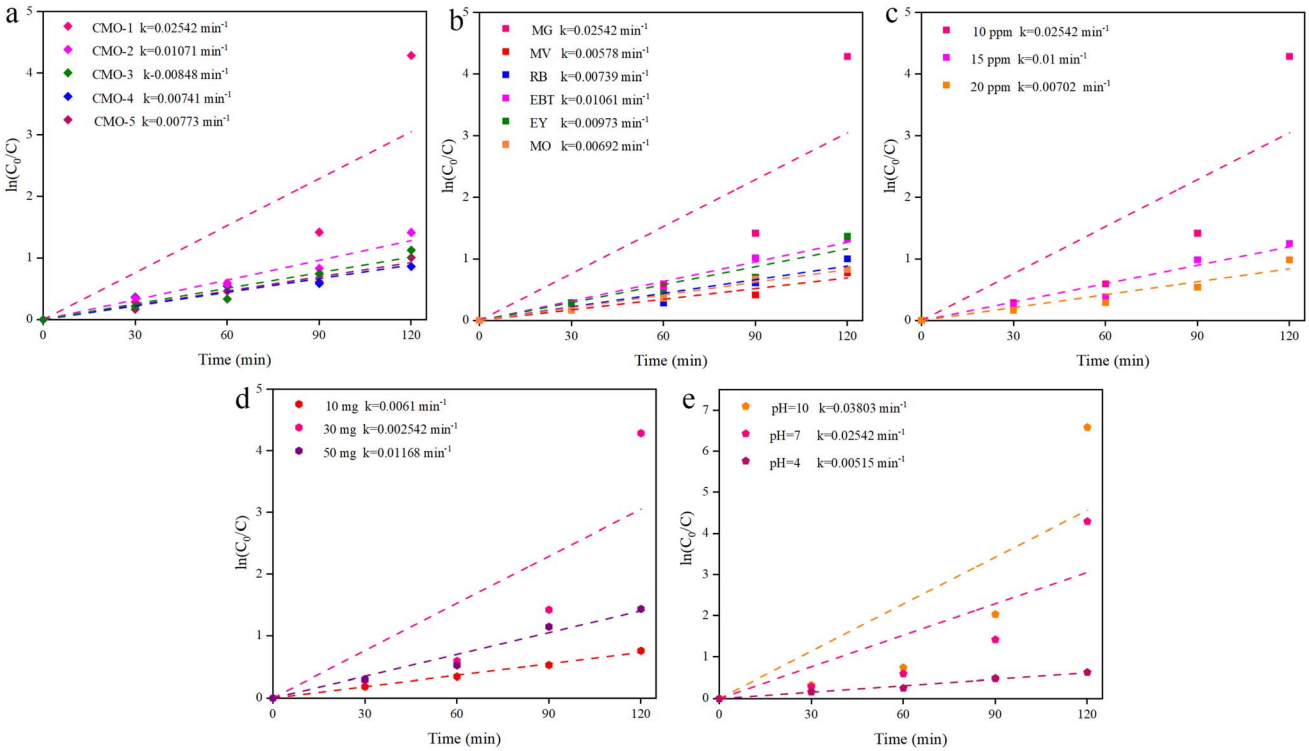

Fig. 9 Kinetics study of (a) different samples of Co_2MnO_4 prepared in different conditions, (b) effect of different organic dyes, (c) effect of different MG concentrations in the presence of 30 mg Co_2MnO_4 prepared in the presence of CA and PG, (d) effect of different dosages of Co_2MnO_4 prepared in the presence of CA and PG over 10 ppm MG, and (e) effect of various pH solution.

was carried out with several amounts of CMO-1 (10–50 mg), as shown. The results showed that degradation efficiency increased with catalyst dosage until 30 mg, which was the most efficient (98.6%). After this dosage level, efficiency remained stable, and by 50 mg it slightly dropped to 76.1% due to too much light scattering and fewer photons on a per active site basis.[23]

The impact of solution pH on malachite green (MG) photocatalytic degradation utilizing Co_2MnO_4 (CMO-1) was systematically evaluated by conducting tests across the pH spectrum within acidic, neutral, and basic conditions (Fig. 8e). The degradation efficiency was strongly dependent on solution pH. Degradation efficiency for alkaline pH (pH 10) was exceedingly high (99.8%), with the degradation efficiency at neutral pH (pH 7) not far behind (98.6% degradation). A notable downside was the degradation efficiency (46.7%) under acidic conditions (pH 4), where MG degradation after the same duration of illumination dropped significantly. It is well-established that degradation efficiency is affected by the photocatalyst surface charge and the ionization state of the dye molecules. At alkaline and neutral pH, the surface of Co_2MnO_4 becomes more negatively charged, which subsequently promotes electrostatic attraction between the catalyst surface and cationic MG dye molecules. There is greater adsorption of the dye on the catalyst surface, thus allowing more effective degradation. In addition, under alkaline conditions, more $^{\bullet}OH$ will be formed because hydroxide ions (OH^-) are more abundant than H^+ and are thus favored. The great amount of OH^- increases the oxidation of MG as the hydroxyl radicals are also very reactive. In acidic conditions, the surface of the catalyst will be positively charged and it will push the positively charged (cationic) dye molecules away due to electrostatic repulsion. Due to this repulsion under acidic conditions, there is less MG on the photocatalyst surface and thus allows less effectiveness of the photocatalytic reactions. Also, when there are low amounts of OH^- ions available there will be low amounts of hydroxyl radicals produced during very acidic conditions. This will decrease or cause the stop of degradation of MG.[24]

The participation of reactive species in the photocatalytic degradation of malachite green (MG) by Co_2MnO_4 (CMO-1) under visible light was studied with selected scavengers and shown in Fig. 8f. Benzoic acid (BA) was used to scavenge hydroxyl radicals ($^{\bullet}OH$), benzoquinone (BQ) was used to scavenge superoxide radicals ($O_2^{\bullet -}$), and EDTA was used to trap the photogenerated holes (h^+).[25] The degradation efficiencies in the presence of these scavengers give insight into the progression of the underlying reaction mechanism. The degradation efficiencies BA and BQ were still high at 94.8% and 96.4%, which suggests that both $^{\bullet}OH$ and $O_2^{\bullet -}$ are only partially reacting species and that both contributions are not the dominant reactions that comprise the photocatalytic pathway. The introduction of EDTA resulted in a considerable degradation reaction efficiency decrease from 98.6% to 59.5%, which supports a model where photogenerated holes are an active mechanism in the degradation reaction. Based on the significant inhibition of activity by EDTA, it is likely that the holes created in the

Table 2 The photocatalytic performance of different compounds

Ref.	Source of light/time (min)	Catalyst dosage (mg)	Dye concentration (ppm)	Highest degradation (%)	Dye	Bandgap (eV)	Catalyst
Present work	Vis/120	30	10	98.6	Malachite green	1.52	Co_2MnO_4
19	Sunlight/60	50	5	87.8	Malachite green	1.70	$CoMn_2O_4$
27	Sunlight/120	0.5	—	92.0	Malachite green	2.54	$CuMn_2O_4$
30	Vis/180	1.0	—	97.0	Brilliant cresyl blue	2.12	Co_3O_4/Fe_2O_3
28	Vis/150	30	20	96.3	Eriochrome black T	2.6	Ni_6MnO_8
31	UV/80	50	—	98.0	Rhodamine B	~3	$NiMn_2O_4$
32	Vis/15	30	20	96.0	Congo red	1.82	$ZnMn_2O_4$
29	UV/120	1	20	60.0	Rhodamine B	1.88	$NiMn_2O_4$/CuS
33	UV/80	5	50	100.0	Methylene blue	—	$CoMn_2O_{3.5}$–RGO
34	Vis/135	20	5	85	Methyl orange	—	Ag/Mn_2O_3
35	UV/300	30	—	96.7	Methylene blue	2.19	$Ni_{0.6}Mn_{0.4}Fe_2O_4$

valence band of Co_2MnO_4 are capable of oxidizing dye molecules directly or promoting secondary reactive oxygen species. The results of the study indicate that the photocatalytic mechanism of CMO-1 under visible light is primarily a hole-based reaction, with $^{\bullet}OH$ and $O_2^{\bullet-}$ radicals contributing to a lesser extent. This agrees with the narrow band gap (1.52 eV) of the material, which facilitates charge separation, further enhancing the valence band holes in driving the reaction.

The practical viability of a photocatalyst relies on its initial activity as well as its stability and reusability under operational conditions for longer periods of time. In order to analyze this possible use of the photocatalyst, recyclability trials were conducted with the CMO-1 sample, which had previously indicated optimal photocatalytic possible performance. In Fig. 8g, the photocatalyst was repeatedly used for five cycles of malachite green (MG) degradation under visible light conditions. After each cycle, the catalyst was recovered through centrifugation, washed, and dried for reuse. The photocatalyst had a slight reduction in degradation efficiency each cycle but maintained degradation above 85.4% in the 5th run from 98.6% in the first run. This slight reduction could be due to the photocatalyst either partially losing material during the recovery phases, or the possible very slight surface fouling due to retained dye intermediates after degradation of MG. Regardless, and even with the slight loss of efficiency in the last trial, the strong retention of activity, once again in a mixed solution for multiple consecutive cycles, suggests the great potential for practical reuse of the Co_2MnO_4 photocatalyst in subsequent environmental remediation-type applications.[26] To confirm that the catalyst was still chemically unchanged after the use through multiple degradation cycles, X-ray diffraction (XRD) analysis was performed on the CMO-1 sample after 5 degradation cycles (Fig. 8h). The peaks in the XRD pattern did not shift significantly, no new peaks appeared, and there were no notable changes in the peak intensities or, hence, the crystallinity. The main reflections related to the spinel phase of Co_2MnO_4 remained without loss or significant alteration, which shows that the catalyst is in a crystalline phase and kept its structure during repeated photocatalytic reactions. The decrease in photocatalytic efficiency after each photoreaction cycle can be attributed to several different factors. The main factors responsible for reducing the photoreaction cycle are the accumulation of degradation products at the catalyst surface, leading to partial coverage; the potential for active site blockage; and the minor loss of reaction catalyst during centrifugation and washing. These types of factors are common in heterogeneous photocatalytic systems and are not necessarily indicative of structural changes.

The kinetic behavior of malachite green (MG) degradation over Co_2MnO_4 nanostructures was investigated using the pseudo-first-order model to extract the rate constants (k) from the $\ln(C_0/C)$ *vs.* time plots (Fig. 9). The results showed the expected relationship between photocatalytic efficiency and rates: those samples or conditions that showed higher degradation percentages also shown higher rates (k). The degradation kinetics for different dyes, concentrations, catalyst dosages, and pH values mirrored the trends observed in the activity tests, validating the consistency and reliability of the results.

Table 2 compares the photocatalytic performance of various manganese-based and composite oxide catalysts (*i.e.* dye degradation efficiency, band gap energy, and operational conditions). Of these catalysts, Co_2MnO_4 catalyst exhibited a defensible degradation efficiency of 98.6% degradation of malachite green dye under visible light in 120 minutes using a reasonable band gap of 1.52 eV and a moderate dose (30 mg) of catalyst. Even with lower doses or shorter exposure times, Co_2MnO_4 outperforms various other reported systems, such as the $CoMn_2O_4$ (87.8%)[19] and $CoMn_2O_4$ (92.0%).[27] Co_2MnO_4 performance also exceeded various materials with higher band gaps, such as Ni_6MnO_8 (96.3%, 2.6 eV,[28]) and $NiMn_2O_4$/CuS (60.0%,[29]). Also, some of these materials, such as $CoMn_2O_{3.5}$–RGO and $Ni_{0.6}Mn_{0.4}Fe_2O_4$ catalysts, achieved complete or near complete degradation of the malachite green dye, but achieved under either UV light sources, or used a higher concentration of dye. Altogether, Co_2MnO_4 would demonstrate very competent visible-light photocatalytic performance due to its narrow bandgap for charge mobility, ease of charge separation efficiencies, and the appropriate morphology and formation during synthesis. Therefore, based on our results Co_2MnO_4 makes a competitive and potentially promising catalyst material for wastewater treatment under a responsible light exposure sustainability.

4. Conclusions

Co_2MnO_4 nanostructures were synthesized using the Pechini technique and showed excellent photocatalytic activity under visible light. The CMO-1 sample achieved 98.6% degradation of malachite green in 120 min and exhibited a pseudo-first-order reaction rate constant of 0.02542 min^{-1}. The narrow band gap (1.52 eV) and narrow range of particle sizes (100–120 nm) provided the effective charge separation, enhancing the surface reactivity. Over 85% of the photocatalyst's initial activity was retained after five successive runs, indicating that the photocatalyst has a stable structure and can be reused. These quantitative results indicate that Co_2MnO_4 has an excellent competitive and sustainable visible-light photocatalyst for wastewater treatment applications.

Conflicts of interest

The authors declare that they have no known competing financial interests or personal relationships that could have appeared to influence the work reported in this paper.

Data availability

The authors confirm that the data supporting the findings of this study are available within the article.

Acknowledgements

The authors gratefully acknowledge the financial support of the University of Kashan (Grant No. 159271/MY5). Authors would also like to acknowledge the partial support received from Ajman University, Internal Research Grant No. [DRG Ref: 2025-IRG-CHS-04].

References

1 Q. Yang, Z. Li, X. Lu, Q. Duan, L. Huang and J. Bi, *Sci. Total Environ.*, 2018, **642**, 690–700.
2 M. Hassan, R. Hassan, M. A. Mahmud, H. I. Pia, M. A. Hassan and M. Uddin, *Urban Reg. Plann.*, 2017, **2**, 13.
3 S. Gupta, S. Satpati, S. Nayek and D. Garai, *Environ. Monit. Assess.*, 2010, **165**, 169–177.
4 S. S. Patil, A. Sukhdev and S. Chandrasekaran, *Opt. Mater.*, 2025, 117101.
5 M. F. Lanjwani, M. Tuzen, M. Y. Khuhawar and T. A. Saleh, *Inorg. Chem. Commun.*, 2024, **159**, 111613.
6 S. T. Fardood, F. Moradnia, S. Ganjkhanlu, L. Ouni, A. Ramazani and M. Sillanpää, *Inorg. Chem. Commun.*, 2024, **167**, 112719.
7 A. Krishnan, A. Swarnalal, D. Das, M. Krishnan, V. S. Saji and S. Shibli, *J. Environ. Sci.*, 2024, **139**, 389–417.
8 D. Wang, X. Chen, D. G. Evans and W. Yang, *Nanoscale*, 2013, **5**, 5312–5315.
9 C. W. Lee, C. Cazorla, S. Zhou, D. Zhang, H. Xu, W. Zhong, M. Zhang, D. Chu, Z. Han and R. Amal, *Adv. Energy Mater.*, 2025, **15**, 2402786.
10 B. He, P. Hosseini, D. Escalera-López, J. Schulwitz, O. Rüdiger, U. Hagemann, M. Heidelmann, S. DeBeer, M. Muhler, S. Cherevko, K. Tschulik and T. Li, *Adv. Energy Mater.*, 2025, **15**, 2403096.
11 N. Rajeevan, P. Pradyumnan, R. Kumar, D. Shukla, S. Kumar, A. Singh, S. Patnaik, S. Arora and I. Shvets, *Appl. Phys. Lett.*, 2008, **92**, 102910.
12 A. N. Naveen and S. Selladurai, *Phys. B*, 2015, **457**, 251–262.
13 N. M. Vaziri and S. Salehipour, *J. Build. Eng.*, 2025, 113907.
14 J. A. M. Mark, A. Venkatachalam and J. p. Jesuraj, *Phys. B*, 2021, **601**, 412349.
15 V. Subha, S. Gowri, R. Kayalvizhi and T. Kamatchi, *J. Inorg. Organomet. Polym. Mater.*, 2025, 1–15.
16 M. Yaqoubi, M. Ghanbari, R. W. Maya, H. A. Jasim and M. Salavati-Niasari, *Results Eng.*, 2025, **25**, 104037.
17 T. L. Le, *Preparation of transition metal oxide thin films used as solar absorbers*, Université Paul Sabatier-Toulouse III, 2016.
18 M. Hosseini, M. Ghanbari, F. H. Alsultany, E. A. Dawi, U. S. Altimari, A. M. Aljeboree and M. Salavati-Niasari, *Inorg. Chem. Commun.*, 2024, **167**, 112749.
19 J. A. M. Mark, A. Venkatachalam, A. Pramothkumar, N. Senthilkumar, K. Jothivenkatachalam and J. Joseph prince, *Phys. B*, 2021, **601**, 412349.
20 S. Aouini, A. Bardaoui, A. M. B. do Rego, A. M. Ferraria, D. M. Santos and R. Chtourou, *Solid State Sci.*, 2023, **143**, 107283.
21 M. Ghanbari, M. Salavati-Niasari and F. Mohandes, *Arab. J. Chem.*, 2022, **15**, 103730.
22 K. M. Reza, A. S. W. Kurny and F. Gulshan, *Appl. Water Sci.*, 2017, **7**, 1569–1578.
23 J. Arshad, F. M. A. Alzahrani, S. Munir, U. Younis, M. Al-Buriahi, Z. Alrowaili and M. F. Warsi, *Ceram. Int.*, 2023, **49**, 18988–19002.
24 F. Yousefzadeh, M. Ghanbari and M. Salavati-Niasari, *Chemosphere*, 2023, **338**, 139564.
25 E. Abkar, A. Al-Nayili, O. Amiri, M. Ghanbari and M. Salavati-Niasari, *Ultrason. Sonochem.*, 2021, **80**, 105827.
26 S. Teixeira, P. Martins, S. Lanceros-Méndez, K. Kühn and G. Cuniberti, *Appl. Surf. Sci.*, 2016, **384**, 497–504.
27 A. Pramothkumar, N. Senthilkumar, K. Jothivenkatachalam, P. Fermi Hilbert Inbaraj and J. Joseph prince, *Phys. B*, 2019, **572**, 117–124.
28 M. Yaqoubi, M. Salavati-Niasari and M. Ghanbari, *Appl. Water Sci.*, 2025, **15**, 20.
29 M. S. Rohokale, D. Dhabliya, T. Sathish, V. Vijayan and N. Senthilkumar, *Phys. B*, 2021, **610**, 412902.
30 S. A. B. Asif, S. B. Khan and A. M. Asiri, *Nanoscale Res. Lett.*, 2014, **9**, 1–9.
31 F. Sedighi, A. Sobhani-Nasab, M. Behpour and M. Rahimi-Nasrabadi, *J. Nanostruct.*, 2019, **9**, 258–267.
32 S. T. Fardood, F. Moradnia and A. Ramazani, *Micro Nano Lett.*, 2019, **14**, 986–991.
33 J.-y. Qu, Z.-q. Yu, Y.-h. Zang, J.-f. Gu, J.-t. Jin and F. Gao, *N. Carbon Mater.*, 2019, **34**, 539–545.
34 S. Elbasuney, A. M. El-Khawaga, M. A. Elsayed, A. Elsaidy, M. Yehia and M. A. Correa-Duarte, *Sci. Rep.*, 2024, **14**, 15658.
35 G. Mathubala, A. Manikandan, S. A. Antony and P. Ramar, *J. Mol. Struct.*, 2016, **1113**, 79–87.